



ALMA Detection of Extreme Blueshifted Ionized Gas within 0.2 pc of Sgr A* from -480 to -300 km s^{-1}

M. J. Royster¹ , F. Yusef-Zadeh¹, M. Wardle² , D. Kunneriath³, W. Cotton³, and D. A. Roberts⁴

¹CIERA and the Department of Physics & Astronomy, Northwestern University, 2145 Sheridan Road, Evanston, IL 60208, USA; mjroyster@u.northwestern.edu

²Department of Physics and Astronomy and Centre for Astronomy, Astrophysics, and Astrophotonics, Macquarie University, Sydney, NSW 2109, Australia

³National Radio Astronomy Observatory, Charlottesville, VA 22903 USA

⁴Fort Worth Museum of Science and History, Fort Worth, TX 76107 USA

Received 2018 September 21; revised 2019 January 7; accepted 2019 January 8; published 2019 February 6

Abstract

We have used the capabilities of the Atacama Large Millimeter/Submillimeter Array to probe the ionized gas toward the Galactic center with the H30 α mm hydrogen recombination line within 30'' of the Galaxy's dynamical center. The observations are made with spatial and spectral resolutions of $0''.46 \times 0''.35$ and 3 km s^{-1} , respectively. Multiple compact and extended sources are detected in the minicavity region with extreme negative radial velocities ranging from -480 to -300 km s^{-1} 2''–3'' (0.08–0.12 pc) from Sgr A*. These are the highest radial velocities of ionized gas detected beyond the inner 1'' of Sgr A*. This new component is kinematically isolated from the orbiting ionized gas. The detected gas has a velocity gradient ranging from -50 to $-200 \text{ km s}^{-1} \text{ arcsec}^{-1}$ located to the southwest of Sgr A* at a position angle of $\sim -160^\circ$. Previous proper-motion measurements in the immediate vicinity of these extreme high-velocity ionized components have been made, and they show transverse velocities that range from 313 to 865 km s^{-1} . If we assume that they are associated with one another, then the total velocity implies these components are gravitationally unbound. In addition, we report the kinematics of cometary radio and infrared sources. These sources are diagonally distributed with a position angle of $\sim 50^\circ$ within 14'' of Sgr A*. We interpret the highly blueshifted features to the southwest where the minicavity is located, and the redshifted cometary sources to the northeast in terms of the interaction of a collimated outflow with an opening angle of $\sim 30^\circ$. An expected mass outflow rate of 2×10^{-7} or $4 \times 10^{-5} M_\odot \text{ yr}^{-1}$ is estimated by a relativistic jet-driven outflow or collimated stellar winds, respectively.

Key words: Galaxy: center – ISM: jets and outflows – radio lines: ISM

1. Introduction

The central parsec of the Galactic center (GC) provides a unique opportunity to gain insight into the extreme physical conditions of Galactic nuclei. At the dynamical center, a supermassive black hole of $4 \times 10^6 M_\odot$ (Reid & Brunthaler 2004; Ghez et al. 2005; Gillessen et al. 2009) is coincident with the compact radio source Sgr A*. On a scale of a few parsecs (1 pc corresponds to 25'' at the 8.5 kpc GC distance), Sgr A* is engulfed by ionized material tracing a mini-spiral structure as well as a ring of molecular gas with a radius of 2–5 pc orbiting Sgr A* at a velocity of $\sim 100 \text{ km s}^{-1}$ (Ekers et al. 1983; Lo & Claussen 1983; Guesten et al. 1987; Jackson et al. 1993; Marshall et al. 1995; Latvakoski et al. 1999; Bradford et al. 2005; Christopher et al. 2005; Herrnstein et al. 2005). It is well known that the bolometric luminosity of Sgr A* due to synchrotron thermal emission from hot electrons in the magnetized accretion flow is several orders of magnitude lower than that expected from the accretion of stellar winds and ionized gas. Over the years, there have been a number of studies to address this puzzling issue using radiatively inefficient accretion flow models in which a fraction of the initially infalling material accretes onto Sgr A* and the rest is driven off as an outflow from Sgr A* (e.g., Quataert 2004; Yuan et al. 2004; Shcherbakov & Baganoff 2010; Wang et al. 2013). Another class of models explaining the low luminosity from accretion onto Sgr A* (in comparison with its expected Bondi–Hoyle accretion rate from nearby gas) considers that most of the gas approaching Sgr A* is pushed away as part of a jet or outflow (e.g., Falcke & Markoff 2000; Das et al. 2009;

Becker et al. 2011; Yusef-Zadeh et al. 2016). Identification of high-velocity, potentially unbound ionized gas clouds tracing the interaction sites of a jet with the surrounding material would provide support for this picture. Our approach is to search for such interaction sites with millimeter hydrogen recombination line (RL) emission from ionized clouds near Sgr A*. High-sensitivity, long-time baseline and broad velocity coverage observations as well as the high line-to-continuum ratio of ~ 2 for the H30 α RL (Zhao et al. 2010; Wilson et al. 2012) provide an unprecedented opportunity to identify and probe interaction sites with extreme kinematics within a parsec of Sgr A*.

One of the earliest high-resolution radio studies of ionized gas in the central parsec was carried out with the Very Large Array (VLA) at 3 cm (Roberts & Goss 1993; Roberts et al. 1996). Radial velocities extending up to -280 km s^{-1} were detected in the minicavity, a circular-shaped structure with a diameter of $\sim 2''$ centered $\sim 3''$ SW of Sgr A* (Yusef-Zadeh et al. 1990). Similarly, IR observations using Br γ and [Ne II] lines have detected a -240 km s^{-1} velocity component in the minicavity region (Lacy et al. 1991; Herbst et al. 1993; Lutz et al. 1993; Krabbe et al. 1995). More recently, two studies at 1.3 cm and 1.3 mm (Zhao et al. 2009, 2010) used the VLA and SMA to fully map the kinematics of the mini-spiral at radio and millimeter wavelengths, respectively. Within a few arcseconds of Sgr A*, they reported enhanced electron temperatures approaching $\sim 1.5 \times 10^4 \text{ K}$. However, their studies were limited by relatively low angular resolution ($1''.9 \times 1''.5$) and focused on radial velocities within $\pm 300 \text{ km s}^{-1}$, which showed similar kinematics to those found in previous radio

RL studies. Measurements in the near-IR with the Very Large Telescope have detected He I, Br γ , and [Fe III] lines, 2''2 south of Sgr A* (Steiner et al. 2013). This localized ionized filament at the eastern edge of the minicavity is highly blueshifted with a peak radial velocity $v_r \sim -267 \text{ km s}^{-1}$ and a velocity gradient of $\sim 200 \text{ km s}^{-1} \text{ arcsec}^{-1}$. There is no obvious stellar source with the same radial velocity to explain the origin of the filament. Steiner et al. (2013) argue that the high-velocity gas is shock-heated and may result from the collision of the northern and eastern arms.

Here we report new Atacama Large Millimeter/Submillimeter Array (ALMA) observations showing multiple highly blueshifted velocity components in the minicavity, one of which has a peak velocity $v_r \sim -455 \text{ km s}^{-1}$ extending to $v_r \sim -480 \text{ km s}^{-1}$. This is the highest blueshifted velocity ionized cloud that has been detected thus far near Sgr A*. Combined with proper-motion measurements, the new components are possibly gravitationally unbound. We also detect RL emission from cometary sources which appear elongated in the direction of Sgr A*. These cometary features are a subset of a number of partially resolved sources (X3, X7, F1, F2, F3, P1, P4, and the Sgr A East tower) that have been detected with radio and $3.8 \mu\text{m}$ observations (Mužić et al. 2007, 2010; Yusef-Zadeh et al. 2012, 2016). These have a mixture of hot dust and ionized gas and are elongated with similar position angles (PAs), $\sim 60^\circ$ and $\sim -120^\circ$ (Mužić et al. 2007, 2010; Yusef-Zadeh et al. 2016). The radial velocity and position-velocity (PV) diagrams are presented. The highly blueshifted features in the minicavity and the cometary sources appear to trace sites of an interaction from a collimated jet- or wind-driven outflow from the direction of Sgr A*.

2. Observations and Data Reduction

The observations were carried out with the ALMA originally as part of a multiwavelength monitoring campaign of Sgr A*. The calibrated Band 6 archival data (project code 2015.A.00021.S) were obtained in Cycle 3 on two epochs, 2016 July 12/13 and July 18/19. We utilized the calibrated data set to extract the H30 α RL in the inner parsec ($\sim 26''$) of the GC at 231.901 GHz with CASA. The data set was first combined along all spectral windows prior to deriving and applying phase self-calibration solutions three times for subsequently shorter solution intervals. A final simultaneous phase and amplitude self-calibration solution was derived for each integration time interval before imaging the continuum.

The H30 α data cube was constructed by first subtracting a linear continuum in the uv plane and then applying the same phase and amplitude solutions derived from the continuum. A broad velocity range of -1200 to $+600 \text{ km s}^{-1}$ was imaged, allowing a search for anomalous high-velocity ($|v_r| > 400 \text{ km s}^{-1}$) emission along with a spectral resolution of 3 km s^{-1} . A Briggs parameter of 0.5 was used to weigh the uv visibilities prior to gridding, which allowed a compromise between natural and uniform weighting schemes that favor extended and compact features, respectively. This achieved a synthesized beam of $0''.46 \times 0''.35$ (PA = $-67^\circ.8$) and a full spectral resolution of 0.63 km s^{-1} . A primary beam correction was applied with a cutoff at 20% ($37''.2$ field of view). The July 12/13 H30 α image cube has $\sigma = 0.4 \text{ mJy}$ per channel, averaged to 3 km s^{-1} .

The continuum was imaged in a similar fashion but was confusion and dynamic range limited with a sensitivity of

$\sigma \sim 0.8 \text{ mJy beam}^{-1}$ and $\sigma \sim 1.6 \text{ mJy beam}^{-1}$ for the July 12/13 and July 18/19 data sets, respectively. Due to the relatively poor data quality of the second epoch, we chose to use only the first (July 12/13) data set in the analysis presented here. However, the high-velocity features described here are also detected in the July 18/19 data set.

The peak continuum position of Sgr A* was found at α, δ (J2000) = $17^{\text{h}}45^{\text{m}}40^{\text{s}}.034, -29^\circ00'28''.190$ in the J2000 reference frame. In order to properly compare to other data sets, we applied a shift to the coordinate system by $+61$ and -123 mas in R.A. and decl., respectively, such that the position of Sgr A* could be found at α, δ (J2000) = $17^{\text{h}}45^{\text{m}}40^{\text{s}}.038, -29^\circ00'28''.069$. Unless otherwise noted, the positions of sources are reported as offsets with respect to this corrected position. All images are displayed in the J2000 coordinate reference system.

3. Results

Figure 1(a) displays a peak intensity image of H30 α at 231.9 GHz. Three prominent components of the mini-spiral are labeled as the northern arm, the eastern arm, and the western arc at the edge of the field of view. A number of compact sources are detected, the most prominent of which is IRS 7, an M2 supergiant star (Lebofsky et al. 1982; Wollman et al. 1982) with a head-tail structure (Serabyn et al. 1991; Yusef-Zadeh & Morris 1991) at PA $\sim 0^\circ$ from Sgr A*. Figure 1(b) shows the velocity of the peak emission of the H30 α RL from the mini-spiral on the same scale and resolution as Figure 1(a). The kinematics of the mini-spiral traced in Figure 1(b) are very similar to past radio and IR measurements (e.g., Roberts & Goss 1993; Roberts et al. 1996; Zhao et al. 2009, 2010; Irons et al. 2012). Broadly speaking the northern arm shows redshifted radial velocity components $v_r \sim 100 \text{ km s}^{-1}$, which gently decreases to $v_r \sim 0 \text{ km s}^{-1}$ from north to south and then makes a large velocity jump to $\sim -300 \text{ km s}^{-1}$ as the gas approaches Sgr A* from the east. The velocity gradient of the eastern arm has an opposite trend, becoming increasingly redshifted before it changes direction and becomes blueshifted ($\sim -200 \text{ km s}^{-1}$) near Sgr A*.

The fourth prominent component of the mini-spiral is within the inner few arcseconds of Sgr A*, the so-called ionized bar. The ionized bar is in fact the high negative velocity component of -200 km s^{-1} which lies closest to Sgr A*. There is a ridge of highly blueshifted gas, with a U-shaped structure (i.e., the minicavity) depressing the continuum emission associated with the ionized bar, where the northern and eastern arms appear to converge. Although the dominant emission is blueshifted, there is also 0 km s^{-1} gas detected throughout this region. Our observations show for the first time highly blueshifted ionized material near Sgr A*, as described below.

3.1. Minicavity

We have found four highly blueshifted velocity components, C1 to C4, along the western and eastern walls of the minicavity. The kinematics of these sources exceed those of the orbiting gas of the ionized bar by $\sim 200 \text{ km s}^{-1}$. Figure 2 shows the distribution of the peak velocity of the minicavity region in H30 α . The four aforementioned sources are labeled and distinguishable by their highly blueshifted $\sim -400 \text{ km s}^{-1}$ emission (blue/teal in the image). The emission from the orbiting gas associated with the ionized bar is shown in red and pink.

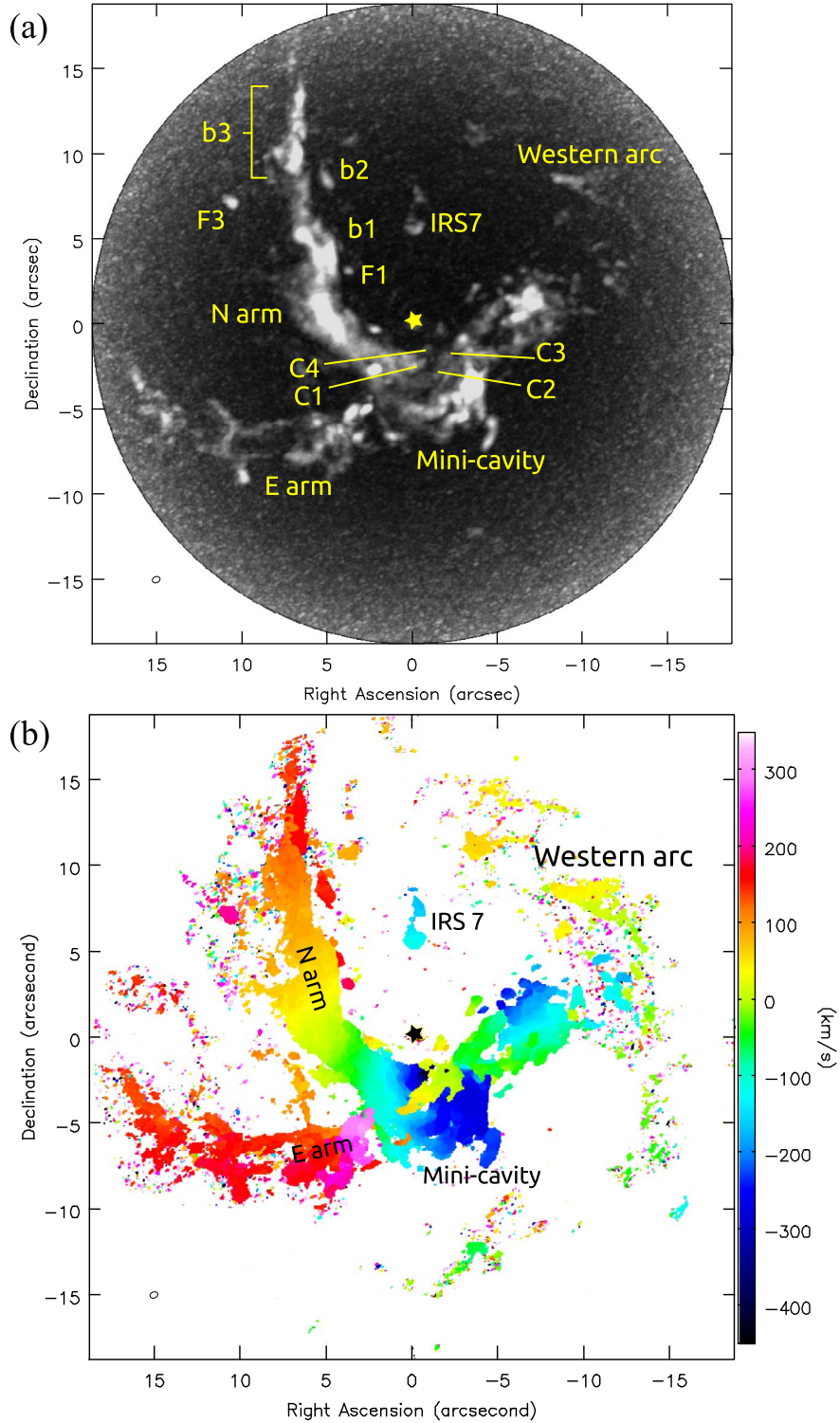


Figure 1. (a) The 231.9 GHz H30 α peak intensity of the mapped region with a synthesized beam, $0''.47 \times 0''.36$ (PA = $-67^\circ 82'$). Coordinates are offset from the position of Sgr A* (yellow star). (b) Velocity coordinates of the peak intensity for H30 α . The position of Sgr A* is designated with a black star.

The PV diagrams along the two slices (arrows in Figure 2) that pass through C1 to C4 are shown in Figure 3. Figure 3(a) (corresponding to the nearly horizontal arrow in Figure 2) shows the kinematic separation of C1, C4, and C3 from the orbiting gas with lower negative velocities. Figure 3(b) shows the PV diagram of C1, C2, and C4, indicating that these sources are also kinematically isolated despite having similar $v_r < -350$ km s $^{-1}$. The individual velocity profiles of

the four components are shown in four panels in Figure 4. C1 shows the highest negative velocity, consisting of (at least) three blueshifted components.

Figure 5 shows nine channel maps of H30 α emission between -380 and -480 km s $^{-1}$. These maps show clearly the blueshifted emission is extended but is confined to the minicavity region. In addition to the aforementioned C sources an additional ridge (yellow dashed ellipse) of ~ -400 km s $^{-1}$

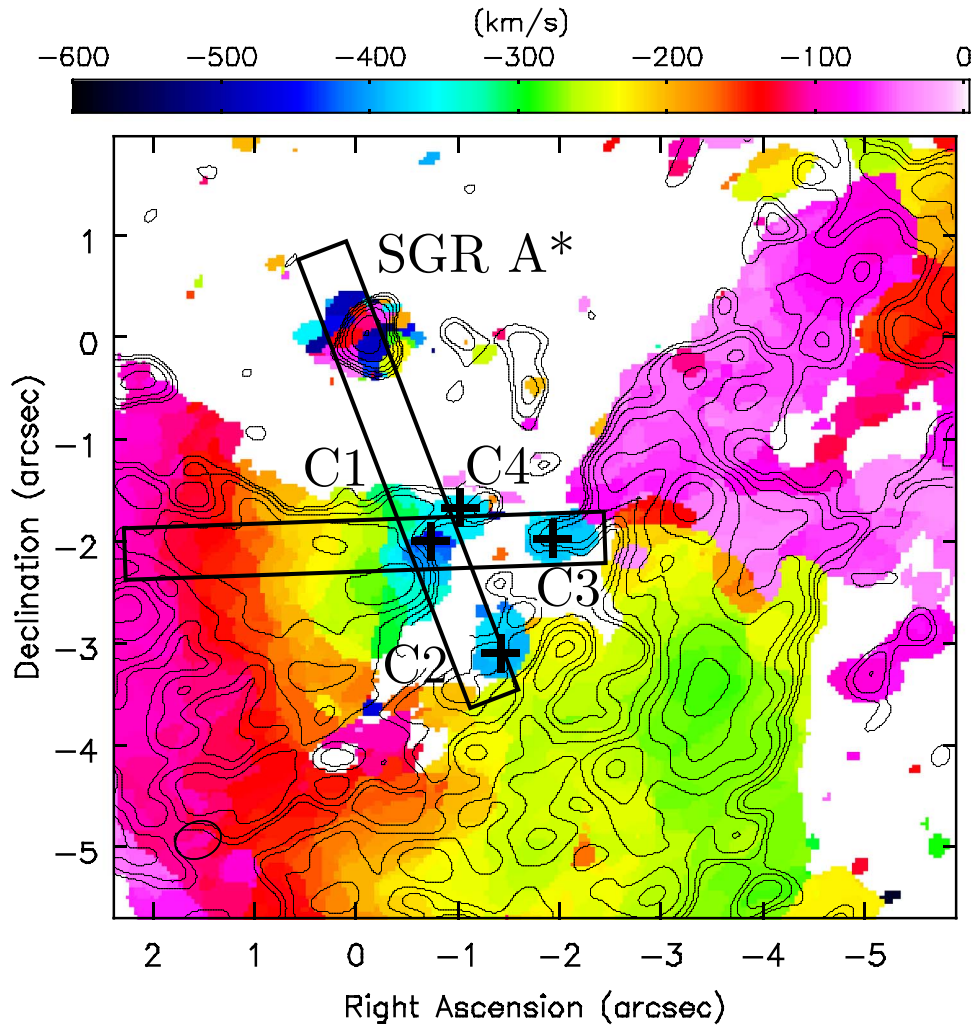


Figure 2. H30 α velocity coordinates for the peak intensity ($>0.2 \text{ Jy beam}^{-1}$) of blueshifted emission in the minicavity region. The contours are the integrated intensities beginning at 0.1 Jy beam^{-1} and increasing by factors of 1.5. The blue/teal-colored emission corresponds to velocities less than roughly -350 km s^{-1} . The four “+” signs are the positions of C1–C4. Each of the two rectangular boxes represents a PV slice found in Figure 3 with a common offset position of α, δ (J2000) = $17^{\text{h}}45^{\text{m}}39^{\text{s}}.98, -29^{\circ}00'30''.25$.

emission is seen in the southwest corner of the minicavity. Because it is coincident with the orbiting gas (seen at velocities $\lesssim 320 \text{ km s}^{-1}$), it is not visible in Figure 1(b). The ridge of emission is most likely He30 α as it is separated by the expected value of 122 km s^{-1} from H30 α emission at -272 km s^{-1} . The He30 α emission was also detected by Tsuboi et al. (2017a). We find $I_{\text{He30}\alpha}/I_{\text{H30}\alpha} \sim 0.8$ in this region, which is typical for H II regions (Wilson et al. 2012).

The positions and physical properties of the individual sources C1–C4 are described below and are summarized in Table 1. The first column of Table 1 is the given source name as described throughout the text. Column 2 is the offset from the position of Sgr A* (see Section 2) in R.A. and decl. Columns 3 and 4 are the projected offset and PA with respect to Sgr A*. Column 5 is an upper limit to the geometric mean of the source. Columns 6, 7, and 8 are the peak intensity, central velocity, and FWHM of the spectra integrated over one synthesized beam, respectively. Note that only relevant (in this case “high-velocity”) components are listed for each source. Column 9 is the lower limit of the electron density for assumed electron temperatures of $(7.5\text{--}12.5) \times 10^3 \text{ K}$ (see Section 3.1.4). For the head–tail sources (see Section 3.2),

column 10 lists the angular length of the structure, and column 11 is the difference in velocity between the head and tail.

3.1.1. C1 and C4

The closest sources to Sgr A* with the highest blueshifted velocities are C1 and C4, which lie at the northeastern corner of the minicavity. C1 is the most prominent of the four high-velocity components defined by the most extreme blueshifted emission. An elliptical Gaussian was fit to the RL integrated intensity from -460 to -450 km s^{-1} . The result was a peak found at $\Delta\alpha = -0''.68, \Delta\delta = -2''.06$ with a projected distance and PA from Sgr A* of $2''.17$ ($\sim 0.09 \text{ pc}$) and -163° , respectively. The top left panel of Figure 4 shows the spectrum at this position. Three velocity components characterize the high-velocity emission, one of which has the highest negative velocity (-455 km s^{-1}) and a line width (FWHM) $\Delta v_r = 37 \text{ km s}^{-1}$, as listed in Table 1. This is the highest-velocity gas found toward the inner parsecs of the GC. In addition the source is notable for a breadth of emission that extends from approximately -460 to -300 km s^{-1} in a $\sim 1''.2$ square region.

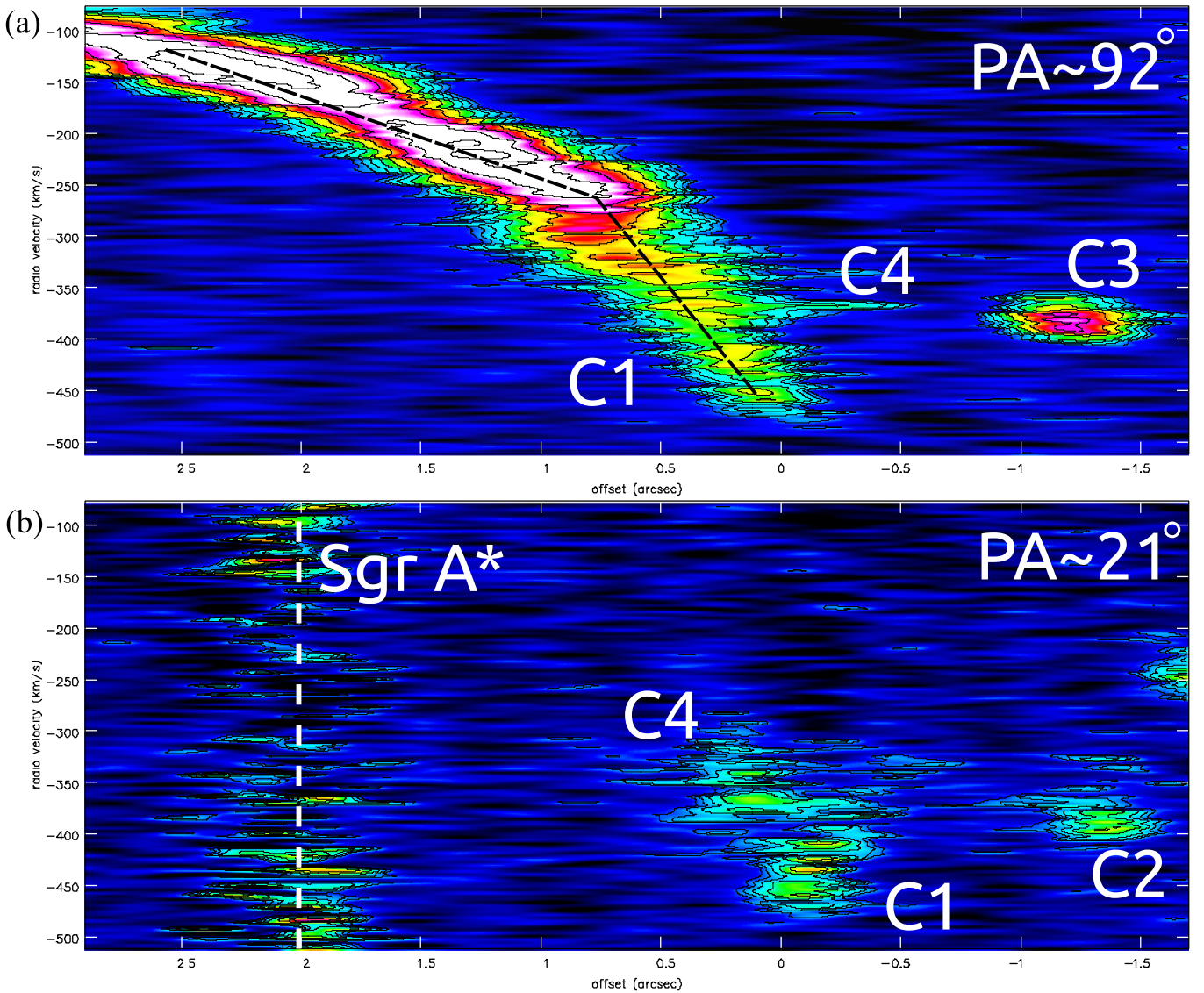


Figure 3. PV slices with zero-offset position taken as α, δ (J2000) = $17^{\text{h}}45^{\text{m}}39^{\text{s}}.98, -29^{\circ}00'30''.25$, while the length of each slice is $4''.7$ and the integrated width is $0''.44$. The given PA (in degrees) is printed in the top right corner of each and corresponds to a box in Figure 2. The position of Sgr A* is represented by a white vertical dashed line in (b). Contours begin at 1 mJy beam^{-1} and increase by factors of 1.3.

The position of C1 is still $\sim 0''.5$ NE of the highest-velocity emission found by Steiner et al. (2013) in the IR. At their position, we find emission that ranges from roughly -415 to -240 km s^{-1} compared to their reported detection at -378 km s^{-1} with [Fe III]. In addition, Tsuboi et al. (2017b) detected $\text{H}42\alpha$ emission at -380 km s^{-1} SW of this position ($2''.8$ from Sgr A*) and attributed it as the counterpart to the high-velocity $\text{Br}\gamma$ emission detected by Steiner et al. (2013).

C4 is defined by the integrated emission from -370 to -360 km s^{-1} , is found to be projected about $0''.5$ NE of C1, and is the closest high-velocity gas to Sgr A* at a distance of $2''.0$ ($\sim 0.08 \text{ pc}$) from Sgr A*. The emission peaks at -366 km s^{-1} , which is less than all three of the fitted components of C1 but is most likely associated with the broad -372 km s^{-1} C1 gas. Both C1 and C4 have a low-velocity component near 20 km s^{-1} with $\Delta v_r \sim 30 \text{ km s}^{-1}$.

Figure 3(b) shows a PV diagram that connects the position of Sgr A* with C1. Because of the nonthermal contribution from

Sgr A*, the continuum is poorly fitted at this position. As a result, there appears to be emission in every channel (the white vertical dashed line). The emission due to C1 is apparent in the panel (located at a $0''$ offset), as is that of C4; however there is no significant contribution of ionized gas between the projected positions of C1/C4 and Sgr A*.

A summary of the velocity gradient is best seen in the PV diagram in Figure 3(a). The velocity gradient in the panel extends from the aforementioned C1 contribution of -460 to -100 km s^{-1} from the northern arm over a projected distance of $\sim 3''$. This yields an overall change of $120 \text{ km s}^{-1} \text{ arcsec}^{-1}$ or $5.0 \text{ km s}^{-1} \text{ pc}^{-1}$. However, a noticeable kink in the ionized emission appears in the PV diagram at an offset of roughly $0''.9$ (to the east). If only positions to the east of C1 (further along the northern arm) are considered, the observed gradient is reduced to $71 \text{ km s}^{-1} \text{ arcsec}^{-1}$, which is more consistent with the orbiting gas of the mini-spiral. However, within $0''.9$ of C1, the velocity gradient is measured as $233 \text{ km s}^{-1} \text{ arcsec}^{-1}$ or

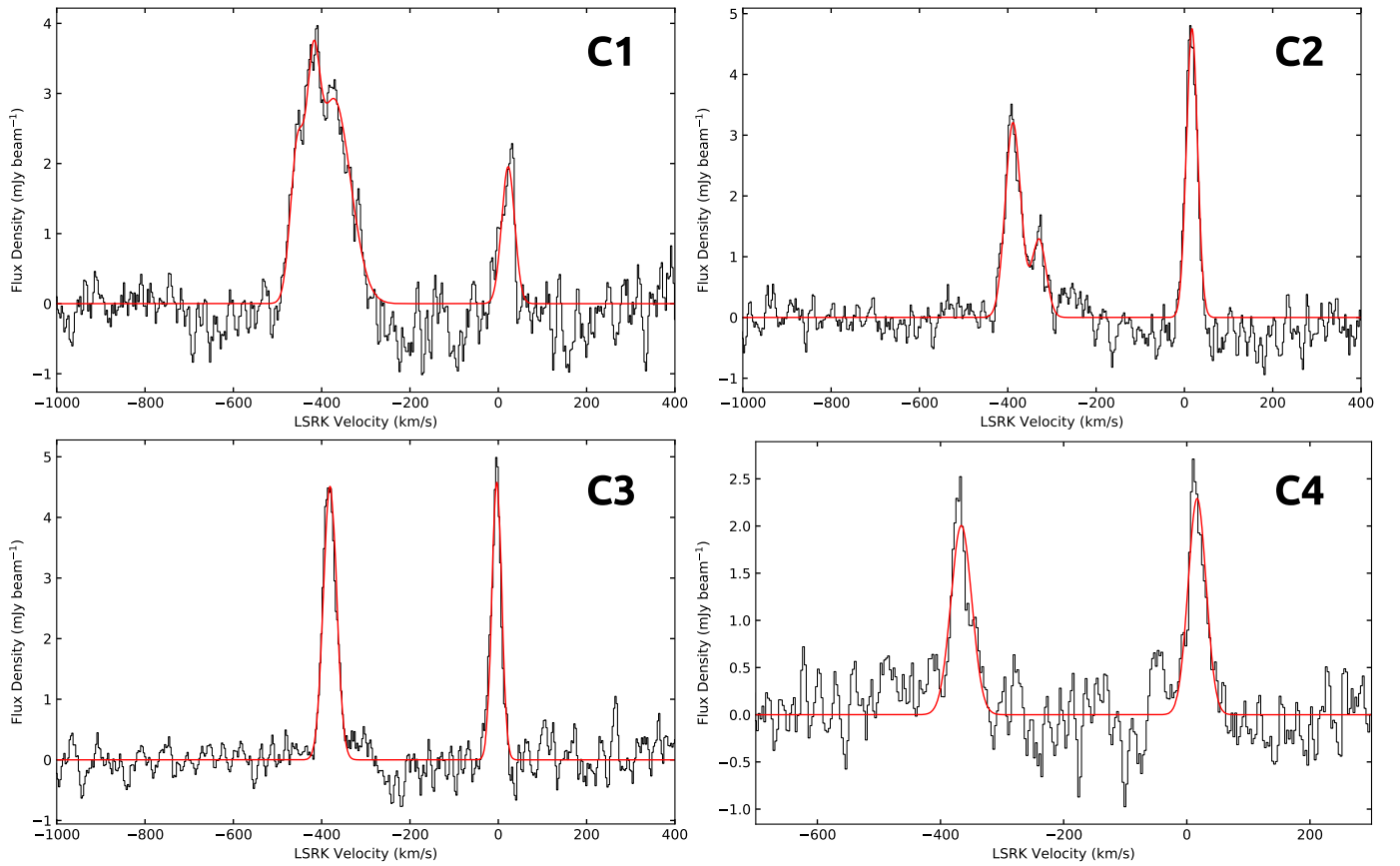


Figure 4. H30 α spectra for each of the four blueshifted sources discussed. Each spectrum is integrated over one synthesized beam ($0''.46 \times 0''.35$) with a spectral resolution of 3 km s^{-1} . The fitted parameters of the blueshifted components are given in Table 1. The $\sim 0 \text{ km s}^{-1}$ component is discussed in the text where applicable.

roughly $10 \text{ km s}^{-1} \text{ pc}^{-1}$. C4 is distinguishable as a small horizontal extension from this increase in velocity gradient.

3.1.2. C2

The C2 source is found toward the projected interior of the minicavity just north of the southern ridge at $\Delta\alpha = -1''.44$, $\Delta\delta = -3''.11$ with a projected angular distance from Sgr A* of $3''.4$. The position was determined with the RL integrated intensity from -400 to -390 km s^{-1} . Notably, a PA from Sgr A* of roughly -155° intersects C1, C2, and C4. This is evident in the PV diagram found in the bottom panel of Figure 3, where the ionized emission of C2 is seen at an offset of roughly $1''.5$. The 2 cm radio continuum source η of Yusef-Zadeh et al. (1990) is coincident with C2.

The H30 α spectra of C2 are shown in Figure 4. Two blueshifted components are measured with the most extreme found with a center velocity of $v_r = -388 \text{ km s}^{-1}$, an FWHM of $\Delta v_r = 41 \text{ km s}^{-1}$, and a peak intensity of $3.2 \text{ mJy beam}^{-1}$. The kinematics are remarkably different from those of the neighboring ionized orbiting gas found just south of C2, where velocities are greater than -250 km s^{-1} . Unlike the C1 source, there appears to be no kinematic connection between the emission and the orbiting gas in the PV diagrams. However, as with C1 (and C4), a low-velocity component is found at $\sim 20 \text{ km s}^{-1}$.

3.1.3. C3

The third of the extreme blueshifted sources is found at $\Delta\alpha = -1''.99$, $\Delta\delta = -1''.96$ just east of the northwestern

corner of the minicavity $2''.8$ from Sgr A*. We have defined C3 by the RL integrated intensity from -390 to -380 km s^{-1} . Similar to C2, C3 appears to be kinematically isolated from the orbiting ionized gas and to be more compact than C1 (see Figure 3). C3 has a peak component at $v_r = -381 \text{ km s}^{-1}$, with $\Delta v_r = 35 \text{ km s}^{-1}$, and an intensity of $4.64 \text{ mJy beam}^{-1}$ (its spectra are shown in Figure 4, and it is in the vicinity of the ζ radio continuum source detected in Yusef-Zadeh et al. 1990). The PA with respect to Sgr A* varies from those of C1 and C2 and is found at roughly -135° . This is a difference of nearly 30° from the C1 PA. Consistent with the other minicavity sources, a low-velocity component is detected, but at -3.3 km s^{-1} instead of 20 km s^{-1} .

3.1.4. The Gas Density

To approximate the electron density (n_e) of the extreme blueshifted emission, nominal values of $7.5 \times 10^3 \text{ K}$ and $12.5 \times 10^3 \text{ K}$ were used for the electron temperature. The electron temperature is known to be elevated near the minicavity (see Roberts & Goss 1993; Zhao et al. 2010), deviating from the typical value of $7.5 \times 10^3 \text{ K}$ for H II regions. The sizes of the sources were determined by fitting an elliptical Gaussian on the plane of the sky where the blueshifted emission was detected. When the source was resolved, we extracted the source size deconvolved from the beam; otherwise it was convolved with the beam. This yields an upper limit on the size of the source or a lower limit on the n_e as calculated below, assuming a path length equal to the upper value.

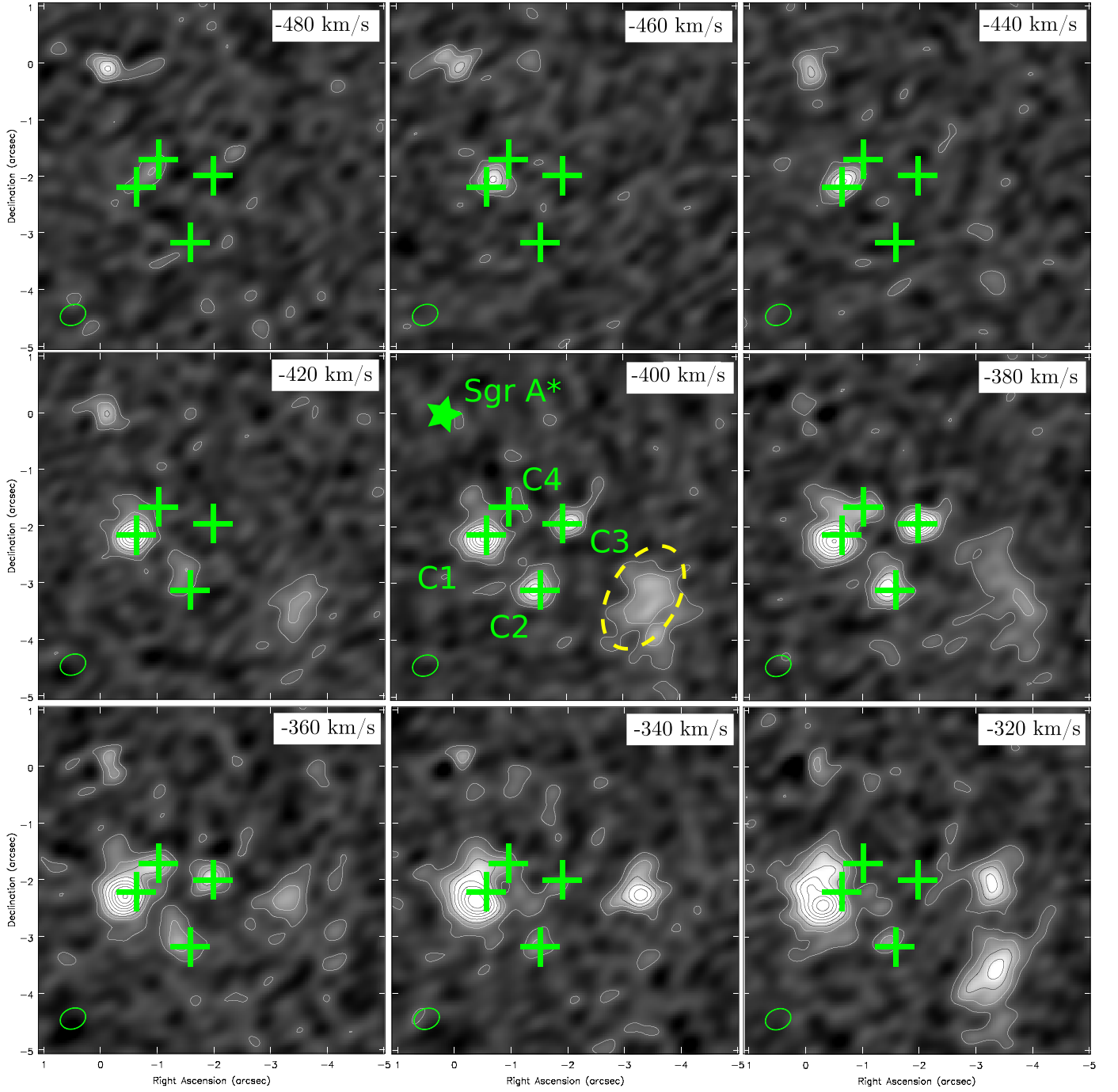


Figure 5. Channel maps of H30 α line emission from the minicavity ($6'' \times 6''$) showing the most negative velocity components with velocity intervals of 20 km s^{-1} . Contours begin at $1.9 \text{ mJy beam}^{-1}$ and increase by factors of 1.2. The “+” signs are the positions of C1–C4, and the star is the position of Sgr A*. The dashed ellipse in the middle panel is the H30 α emission mentioned in Section 4.1.

The line intensity at 231.9 GHz can be expressed as (Wilson et al. 2012):

$$T_L = 1.92 \times 10^3 \left(\frac{T_e}{\text{K}} \right)^{-3/2} \left(\frac{\text{EM}}{\text{cm}^{-6} \text{ pc}} \right)^{-1} \left(\frac{\Delta\nu}{\text{kHz}} \right) \text{K}. \quad (1)$$

Solving for the emission measure (EM) while converting to velocity space and flux density,

$$\text{EM} = 5.71 \times 10^{-2} \left(\frac{T_e}{\text{K}} \right)^{3/2} \left(\frac{S_L}{\text{mJy}} \right) \left(\frac{\Delta\nu_r}{\text{km s}^{-1}} \right) \text{cm}^{-6} \text{ pc}, \quad (2)$$

dividing by the path length, and taking the square root then gives us the n_e . Most of the RL emission observed was best characterized with multiple velocity components. Thus to apply Equation (2) we interpreted the last two factors as the sum of the product of each (blueshifted) component, $\sum(S_L \Delta\nu_r)$.

The estimated (lower limit) n_e is given in Table 1 for both values of the assumed T_e with the path length taken to be identical to the source size projected on the sky. C1 is found to have a much higher density with a value of $\sim(3.4\text{--}5.0) \times 10^4 \text{ cm}^{-3}$ than the other minicavity sources. C3 and C4 have a much lower range of $(1.4\text{--}2.7) \times 10^4 \text{ cm}^{-3}$. The n_e of C2 is

Table 1
H42 α Minicavity and Cometary Sources

Source	$\Delta\alpha, \Delta\delta$ (J2000) ^a (arcsec)	Offset ^a (arcsec)	PA ^a (deg)	Size (mas)	S_L (mJy)	v_r (km s ⁻¹)	Δv_r (km s ⁻¹)	n_e^b (10 ⁴ cm ⁻³)	Length (arcsec)	$ \Delta V $ (km s ⁻¹)
C1	-0.68, -2.06	2.17	-163	320	2.06	-455	37.0	3.39–4.97		
					2.24	-419	33.1			
					2.92	-372	89.0			
C2	-1.44, -3.11	3.43	-155	180	3.21	-388	41.1	2.99–4.39		
					1.28	-329	37.9			
C3	-1.99, -1.96	2.80	-135	420 ^c	4.51	-381	35.7	1.85–2.72		
C4	-0.99, -1.72	1.99	-149	390 ^c	2.01	-366	40.0	1.36–1.99		
F1	+3.89, +3.07	4.95	51.7	390 ^c	6.42	181	26.4	1.97–2.89	0.5	8
F3	+10.7, +7.08	12.8	56.5	580	11.8	196	22.1	2.01–2.94	0.7	6.7
b1	+4.29, +4.42	6.16	35.7	480	2.92	166	31.0	1.30–1.91	0.3	6.6
b2	+5.04, +8.20	9.63	31.6	530	7.09	152	25.6	1.75–2.57	0.69	3.67
b3	+6.76, +11.7	13.5	30.0	930	10.4	164	22.9	1.51–2.22	2.1	8.2

Notes.

^a With respect to Sgr A* (α, δ (J2000) = 17^h45^m40^s.038, -29°00′28″.069).

^b Assuming electron temperatures ranging from 7.5×10^3 to 12.5×10^3 K.

^c Unresolved; the given size is an upper limit convolved with the beam.

comparable to that of C1, but it should be noted that the assumed size of C2 is nearly half that of C1.

To approximate the *total* mass of the extreme blueshifted emission coincident with the minicavity, the entire region that contained significant emission from -500 to -300 km s⁻¹ was integrated. The region is equivalent to 11.7 beams (1.5 arcsec²) at roughly $\Delta\alpha = -1''.05$, $\Delta\delta = -2''.36$. This velocity range accounts for the peaks of negative velocity components as well as the width seen due to thermal and turbulent broadening. The resultant spectra of the blueshifted emission were best fit with two Gaussians at -353 and -264 km s⁻¹. The more negative component has a peak and FWHM of 1.8 mJy beam⁻¹ and 131 km s⁻¹, respectively. Applying Equation (2), we determined an EM of roughly 1.3×10^7 cm⁻⁶ pc from this negative component.

The geometric mean of the area of the integrated region was used as the path length; this corresponds to 1''.2 or 0.05 pc, which is roughly the diameter of the minicavity. If a nominal value of 10⁴ K for the electron temperature is assumed, then an average electron density of 1.6×10^4 cm⁻³ and a total mass of 0.052 M_\odot for the highly disturbed ionized gas in the minicavity are determined.

3.2. Cometary Sources

To the northeast of Sgr A*, a number of previously detected cometary sources were detected in H30 α RLs. Figure 6 is an integrated intensity map from 150 to 190 km s⁻¹ with the detected cometary sources labeled in relation to Sgr A*. PV diagrams of the five sources can be found in Figures 7 and 8.

3.2.1. F Sources

F1 and F3 are known cometary sources pointed in the direction of Sgr A*. These cometary tails are associated with dusty stars that have been detected in the radio band (Yusef-Zadeh et al. 2016). The PAs (with respect to Sgr A*) of F1 and F3 (52° and 55°, respectively) are similar to those of two other IR-identified cometary sources—X3 and X7, found to the southwest of Sgr A* (Mužić et al. 2007, 2010)—and of the minicavity source C3 discussed in Section 3.1.3.

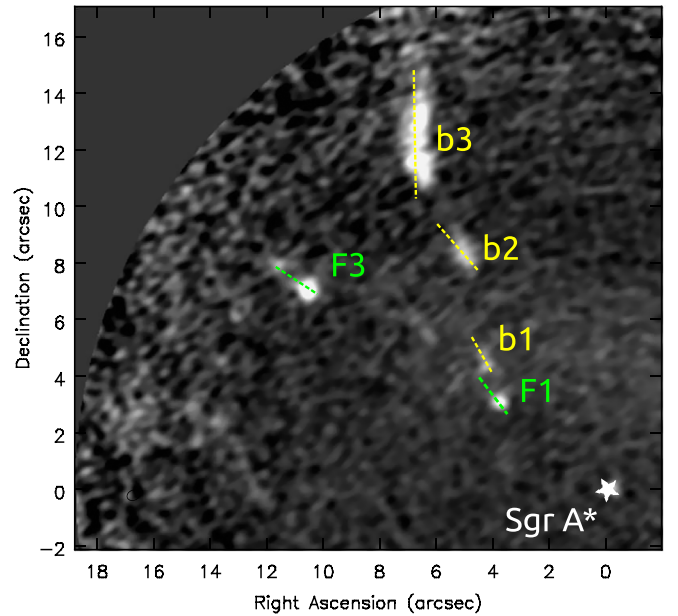


Figure 6. An H30 α integrated intensity map from 150 km s⁻¹ to 190 km s⁻¹. All the F and b sources are visible in this range. A dashed line represents a corresponding PV diagram in Figures 7 and 8. The F1 and F3 PAs (green-colored) are 36° and 57°, respectively. The b1, b2, and b3 PAs (yellow-colored) are 30°, 41°, and 0°, respectively.

The radial velocities of these dusty sources were derived from their H30 α emission, and the parameters that characterize these sources are described in Table 1. Electron densities of $\sim 2 \times 10^4$ cm⁻³ are determined if an electron temperature of 7.5×10^3 K is assumed. The PV diagrams of F1 and F3 (Figure 7) show that the tail, pointed in the direction away from Sgr A*, is more redshifted than the head of the source. PAs of 36° and 55° were adopted for the PV slices of F1 and F3, respectively, which match the morphological orientation of the cometary sources in the *L'*-band data (Mužić et al. 2007). For the F1 cometary source, the kinematics vary from 179 km s⁻¹ at the head to 187 km s⁻¹ at the tail across an angular distance of 0''.5. Similarly, F3 varies from 191 km s⁻¹ to 198 km s⁻¹ over 0''.7.

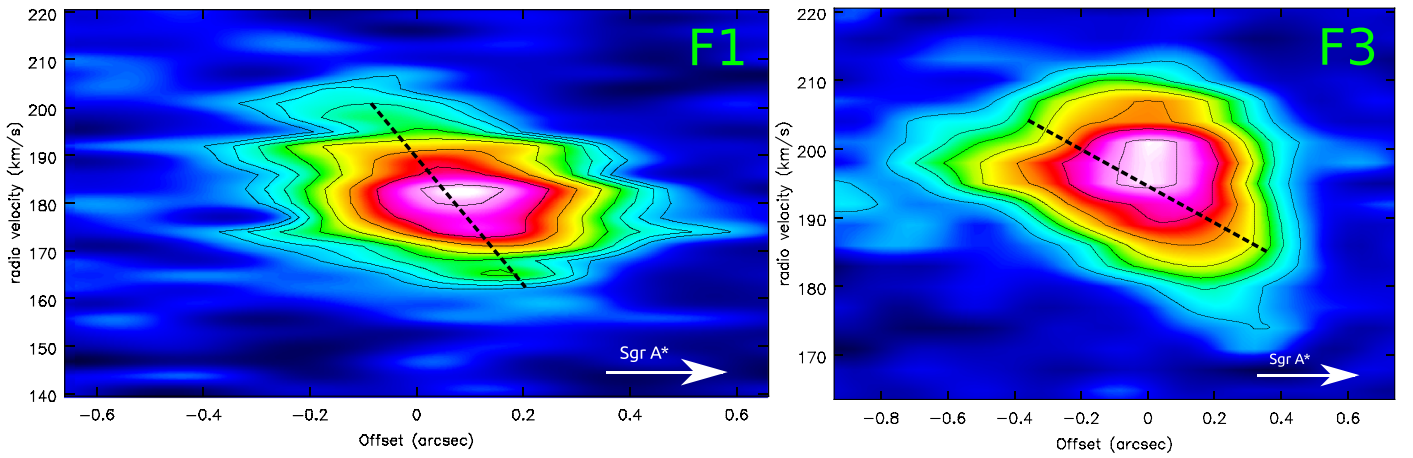


Figure 7. H30 α PV diagrams for the F sources to the northwest of Sgr A*. Left: H30 α F1 PV diagram. The zero-offset position (α , δ (J2000) = 17^h45^m40^s.33, -29° 00'25".05) was determined by fitting the H30 α peak position. The PA of the slice was taken to be that of the *L*-band cometary source (Mužić et al. 2010) of 36°22'. Sgr A* is at a PA of 51°7' from the zero-offset position (F1). The width of the PV slice was 0".44. Contours begin at 1.2 mJy beam⁻¹ and increase by factors of 1.25. Right: H30 α F3 PV diagram with zero offset at α , δ (J2000) = 17^h45^m40^s.83, -29°00'21".12 obtained using an integrated H30 α intensity and with a PA with respect to Sgr A* of 56°5' (also used as the PA of the slice). Contours begin at 0.7 mJy beam⁻¹ and increase by factors of 1.25. A width of 0".6 was used.

3.2.2. *b* Sources

There are also a number of additional cometary sources seen in ionized gas (b1, b2, and b3 in Figure 6) that run nearly parallel to the northern arm of the mini-spiral. The PV diagram of each can be found in Figure 8. It is not clear if any of the *b* sources have stellar counterparts. The general velocity structure differs from that of the *F* sources, which have a redshifted tail. The overall direction is pointed toward Sgr A*; however the PA of the head–tail structure does differ from those of F1 and F3, as they are rotated toward the direction of F1.

The first of the sources, b1, is separated from F1 by roughly 1".3 and is blueshifted with respect to F1 with $v_r \approx 165$ km s⁻¹. The source is the weakest of the discussed cometary sources with a peak intensity of 2.92 mJy. Over an angular distance of 0".3 we find a shift in velocity of 6.6 km s⁻¹ with a redshifted tail, similar to those of the *F* sources.

The remaining two, b2 and b3, both have a velocity gradient with a redshifted head. These appear to potentially be part of a coherent source distinct from the northern arm, whose kinematic structure opposes b2 and b3 (see Figure 1(b)). b2 is roughly 10" from Sgr A* with a central velocity of 152 km s⁻¹. Elongated over an angular distance of $\sim 0".9$ and a PA = 41°, b2 varies by 3.7 km s⁻¹. b3 is found further to the north, 13".5 from Sgr A* and extended over 2"–3", coincident with the northwestern ridge of the northern arm. A velocity gradient of 3.9 km s⁻¹ arcsec⁻¹ was measured.

4. Discussion

4.1. Unbound Minicavity

We have detected highly blueshifted ionized gas with radial velocities ranging between -480 and -300 km s⁻¹. This gas is distributed in a region between 2".0 and 3".5 from Sgr A*. The high-velocity features are partially resolved and are physically associated with the minicavity ridge with a 2" circular-shaped diameter. The minicavity is embedded within the ionized bar, which is dominated by the orbital motion of the gas. Proper-motion measurements of the eastern and western edges of the minicavity show transverse velocities moving southwest and west, respectively (Yusef-Zadeh et al. 1998; Zhao et al. 2009). In one study, the regions roughly coincident with the edges of

the eastern and western walls of the minicavity show transverse velocities ranging between -496 ± 97 and 804 ± 255 km s⁻¹ (boxes 2 and 8 in Table 1 of Yusef-Zadeh et al. 1998).

More recent proper-motion measurements by Zhao et al. (2009), with much improved signal-to-noise data, show consistently high transverse velocities in the minicavity region. When combined with the high radial velocities of the ionized gas detected here, the possibility of unbound components becomes likely. The ionized gas is gravitationally responding to a $4 \times 10^6 M_\odot$ central source, Sgr A*. Although a central stellar population could also contribute, the mass profile of the inner parsec is flat as derived from stellar kinematics (Fritz et al. 2016). Thus, the escape velocity at a *projected* distance of 0.09 pc (2".2) is ~ 620 km s⁻¹. For C1 to be unbound then, it must have a transverse velocity $\gtrsim 420$ km s⁻¹. Note that the actual requirement is lower as the true distance from Sgr A* likely exceeds the projected distance.

Alternatively C1 may be contained in an eccentric Keplerian orbit around Sgr A*, $v_{\text{orbit}} = \sqrt{\frac{GM}{r}}(1 + e) \sin i$. If we make the assumption of an orbital inclination of $i = 90^\circ$, then $v_{\text{orbit}} = v_r = 455$ km s⁻¹, which requires an eccentricity of $e \gtrsim 0.11$. However, it should be noted that in addition to the assumption of zero transverse velocity, the orbit would also be at perihelion in this scenario.

As an example of proper motions, consider the K25 and K33 sources (see Table 2 of Zhao et al. 2009), which are 0".52 and 0".41 away from C1 (within one resolution element) with transverse velocities of 865 km s⁻¹ and 313 km s⁻¹, respectively. When these are added to the -455 km s⁻¹ radial component of C1, we find a total velocity of 988 km s⁻¹ and 552 km s⁻¹ for K25 and K33, respectively. Thus, if we assume C1 has similar transverse velocities to these closest H II knots studied in Zhao et al. (2009), then C1 is unbound. In the case of C1 being coincident with K25, this would be true considering the projected distance alone.

The other minicavity sources (C2 and C3) have similar escape velocities of 500 and 540 km s⁻¹, respectively, at their projected distances. C3 is found adjacent (0".22 apart) to the K32 source of Zhao et al. (2009) with a reported transverse velocity of 656 km s⁻¹, which already places it in the unbound regime. The K41 source of Zhao et al. (2009) is nearly

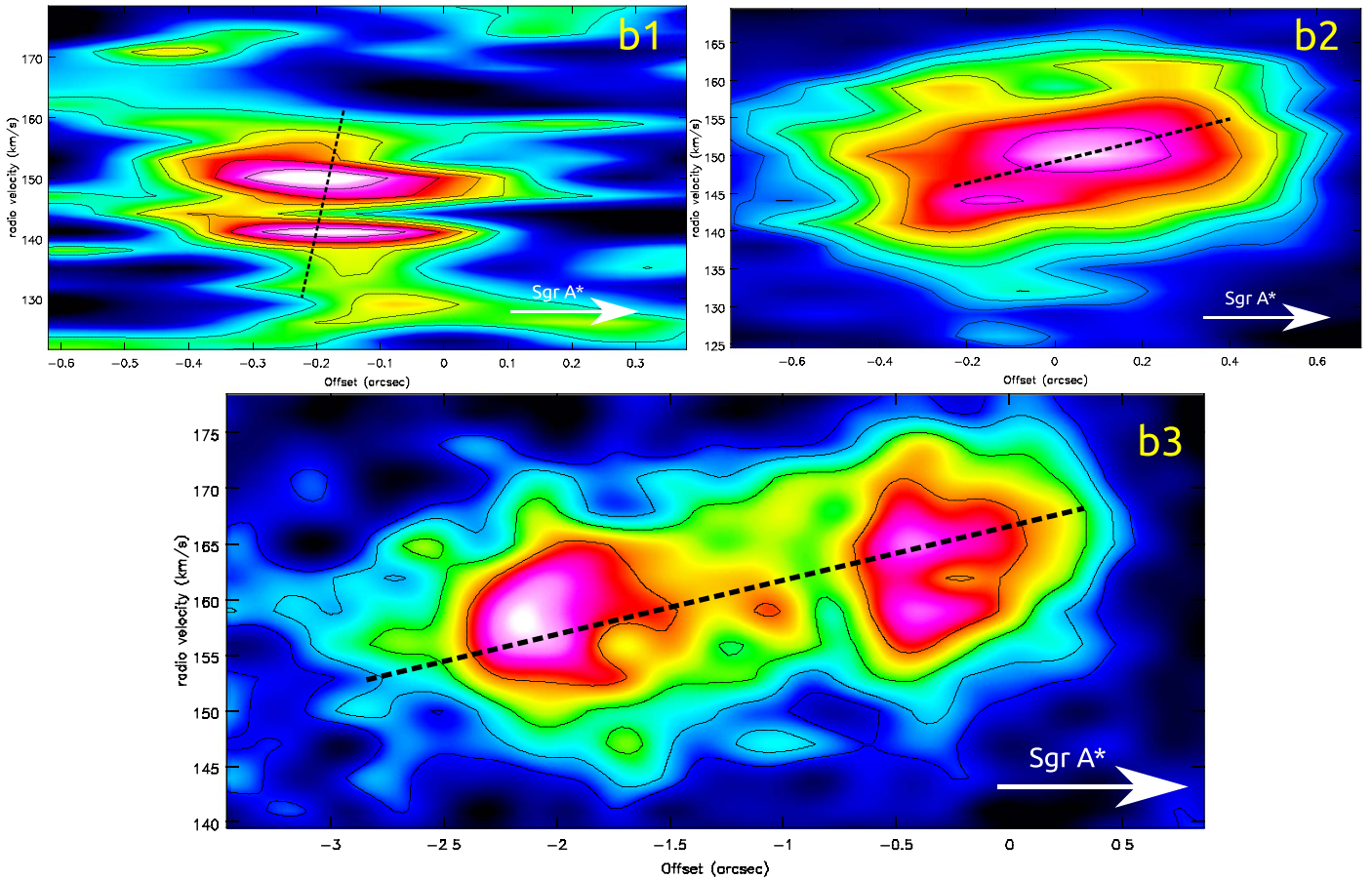


Figure 8. H30 α PV diagrams for the b sources to the northwest of Sgr A*. Top left: H30 α b1 PV diagram with zero offset at α, δ (J2000) = $17^{\text{h}}45^{\text{m}}40^{\text{s}}36, -29^{\circ}00'23''80$ obtained by fitting H30 α emission at 170 km s^{-1} . PA = $29^{\circ}95$, matching the orientation of the cometary source. Contours are based on $2\sigma = 2 \times 0.7 \text{ mJy beam}^{-1}$ and increase by multiples of 1.25. A width of $0''.4$ was used. Top right: H30 α b2 PV diagram with zero offset coincident with the peak position of 150 km s^{-1} emission at α, δ (J2000) = $17^{\text{h}}45^{\text{m}}40^{\text{s}}42, -29^{\circ}00'19''80$ with PA = $41^{\circ}40$. Contours begin at $0.8 \text{ mJy beam}^{-1}$. A width of $0''.75$ was used. Bottom: H30 α b3 PV diagram with zero offset at α, δ (J2000) = $17^{\text{h}}45^{\text{m}}40^{\text{s}}56, -29^{\circ}00'16''32$. A width of $1''.0$ was used, and the cut was along a 0° PA.

coincident with C2 ($0''.13$ away) and has a reported transverse velocity of 215 km s^{-1} . When this is added to the measured C2 radial velocity, a total velocity of 444 km s^{-1} is found. Thus, if the projected distance of C2 is the true distance, it is not necessarily unbound. However, if a true distance of at least 0.18 pc is assumed (versus the projected distance of 0.14 pc), the velocity of the ionized gas would exceed the escape velocity. Such a true distance would require an inclination of 38° between Sgr A* and C2.

4.2. Origin of High-velocity Gas

Steiner et al. (2013) did not find any stellar sources with radial velocities similar to that of high-velocity ionized gas. The large extent and multiple velocity components of blueshifted gas are consistent with the picture that stars are not responsible for originating high-velocity gas. The origin of high-velocity gas is argued to be collisions between the gases of the northern and eastern arms (Steiner et al. 2013; Zhao et al. 2009). However, the U-shaped morphology of the minicavity embedded in the bar is difficult to explain in this picture both spatially and kinematically. Both the northern and eastern arms have velocities that are lower than the high velocities that are reported here.

The new measurements show that the ionized bar is kinematically disturbed in the region traced by the minicavity

ridge. Also, the highest ratio of [Fe III] to the radio continuum in the inner $5''$ of Sgr A* coincides with the minicavity (Eckart et al. 1992; Lutz et al. 1993). This high ratio indicates that the gas is shocked and the [Fe III] line emission traces the shock destruction of dust (Lutz et al. 1993). In addition, the high electron temperature, gas density, and unbound gas associated with the minicavity make this source unique in terms of morphology, kinematics, and thermodynamics. These measurements provide compelling evidence that the gas in the bar is tracing an interaction site due to a jet- or wind-driven outflow from the direction of Sgr A*. The outflowing material is responsible for sweeping up the interstellar material, creating a cavity within the bar of ionized gas.

On a larger scale, the head-tail sources (e.g., F1 and F3) at PAs of 52° and 57° , as well as a striking tower of nonthermal radio emission at PAs $\sim 50^{\circ}$ – 60° (see Yusef-Zadeh et al. 2016), have also been argued to be sites of interaction with the atmosphere of dusty stars driven by a collimated outflow by winds or a jet from Sgr A*. In this picture, the acceleration of the tail to higher positive velocities constrains the geometry of the outflowing material, implying that the cometary sources lie on the farside of Sgr A*.

The picture we propose is similar to previous collimated outflow models argued in Yusef-Zadeh et al. (2012, 2016) and Lutz et al. (1993) to explain the origin of highly blueshifted

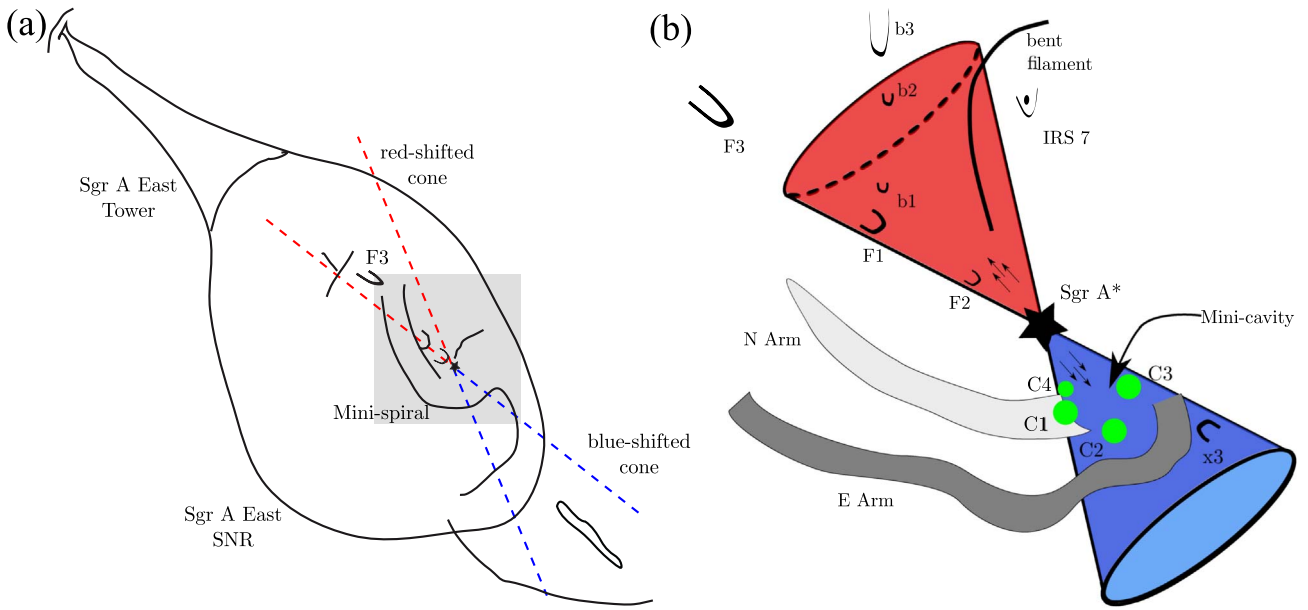


Figure 9. (a) A broad schematic of the mini-spiral and Sgr A East supernova remnant. (b) A schematic showing the details of the shaded region of (a). The green circles represent the four C sources discussed in the text. The red (blue) shading of the cone is the candidate jet-like feature moving away from (toward) the observer. The nearside of the jet is blueshifted and interacts with the minicavity. Meanwhile, the redshifted component is on the farside of Sgr A* and behind the northern arm but possibly interacts with the cometary features discussed.

gas. The collimated outflow is generated either by the winds of massive young stars (e.g., Paumard et al. 2006; Lu et al. 2009) distributed within ~ 0.2 pc of Sgr A* or from Sgr A* itself. The model of a nuclear wind from a cluster of massive stars has to punch through the ionized bar and create the minicavity. This implies that the cluster wind has to be anisotropic. However, this scenario appears to be inconsistent with the jet proposed by Li et al. (2013) based on a linear X-ray feature that they detected. The X-ray jet candidate is asymmetric and oriented in the direction toward the eastern arm, which is roughly perpendicular to the model discussed here.

If the outflow originates from Sgr A^{*}, the highly disturbed and blueshifted gas is a result of a mildly relativistic jet symmetrically emanating from Sgr A^{*}. The blueshifted component of the jet is on the nearside of Sgr A^{*} and punches through the orbiting gas in the ionized bar, which results in the observed structure of the minicavity. This also places the ionized bar on the front side of Sgr A^{*}. The farside (redshifted component) of the jet interacts with the atmosphere of the dusty cometary sources toward Sgr A^{*}, creating a more redshifted tail in the direction of Sgr A^{*}. We also consider the possibility that the farside of the jet interacts with the Sgr A East supernova remnant and creates the Sgr A East tower, 150'' away from Sgr A^{*} with a PA $\sim 50^\circ$ – 60° (Yusef-Zadeh et al. 2016). In this picture, the northern arm is aligned close to the plane of Sgr A^{*} so that the interaction of the orbiting ionized gas of the mini-spiral and the jet only occurs on the nearside of Sgr A^{*}. Such an alignment is consistent with previous RL studies using the Keplerian model (Zhao et al. 2009). A schematic diagram in Figure 9(a) shows the large-scale structures, including the aforementioned Sgr A East tower. Smaller-scale features are displayed in Figure 9(b). The suggested symmetric jet-driven outflow is colored in the schematic to illustrate the radial direction of flow for each side.

4.3. Mass Outflow Rate

We now quantify the mass outflow rate required to produce the minicavity. The blueshifted ionized bar lies in the nearside of the

plane of the sky before the jet accelerates the gas to more negative velocities. The change in the velocity of the gas due to this puncture is about 200 km s^{-1} over a projected angular distance of $\sim 1''$ (see Figure 3). If the total mass of the disturbed gas found in Section 3.1.4 as $\sim 0.052 M_{\odot}$ is utilized, then we can estimate the momentum deposition rate as $0.051 M_{\odot} \text{ yr}^{-1} \text{ km s}^{-1}$. Adopting a Lorentz factor of $\gamma \sim 2.7$ for the mildly relativistic jet, a mass outflow rate of $1.8 \times 10^{-7} M_{\odot} \text{ yr}^{-1}$ would satisfy a jet origin for the minicavity.

Alternatively, if the outflow is driven by winds from massive stars, the required mass-loss rate is $4 \times 10^{-5} M_{\odot} \text{ yr}^{-1}$ assuming a wind velocity of $\sim 1.25 \times 10^3 \text{ km s}^{-1}$. The global wind accelerating C1–C4 and creating the minicavity has to be anisotropic with a total mass-loss rate much higher than estimated here.

The cometary sources can also be utilized to check for consistencies in a collimated outflow model with arguments similar to those above. However, the change in velocity from the head to the tail over the angular distance (Section 3.2 and Table 1) is used to determine the force or momentum deposition rate imparted onto the cometary source that is moving within the candidate outflow. For the F sources a total mass of 1.6×10^{-3} and $5.4 \times 10^{-3} M_{\odot}$ was found for F1 and F3, respectively.

Unlike the minicavity structure, however, the cometary sources only subtend a small fraction of the collimated outflow because they are more than a few arcseconds from Sgr A*. We adopt an opening angle for this outflow of 30° determined by considering the PA difference between C1 and C3. Similar cometary sources (X3 and X7) have been modeled by Mužić et al. (2010), where a size of a few hundred astronomical units was determined for the bow shock standoff distance. Thus, a reasonable estimate for the upper limit of the cross-sectional size of the mid-IR stellar source is 50 au. These parameters yield total mass outflow rates of 3.8×10^{-6} and $4.3 \times 10^{-5} M_\odot \text{ yr}^{-1}$ for a collimated jet, whereas a wind-driven outflow would have to drive $\sim 10^{-4} M_\odot \text{ yr}^{-1}$.

Both b1 and b2 imply mass outflow rates similar to those of the cometary sources. For a collimated jet, mass outflow rates




of 8.5×10^{-6} and $3.8 \times 10^{-6} M_{\odot} \text{yr}^{-1}$ are required if it is responsible for b1 and b2, respectively. On the other hand, b3 requires a much higher outflow rate of $7.4 \times 10^{-5} M_{\odot} \text{yr}^{-1}$ and a highly unlikely wind mass-loss rate of $0.02 M_{\odot} \text{yr}^{-1}$. The larger estimates required for b3 are most likely due to its particularly elongated morphology. However, this most likely suggests b3 does not interact with the proposed collimated outflow and is caused by different mechanisms.

4.4. Summary

Multiple highly blueshifted disturbed features of ionized gas have been detected. The high-velocity sources are associated with the minicavity within $2''$ of Sgr A*. In addition we obtained the kinematics of cometary sources pointing in the direction of Sgr A*. These measurements suggest a collimated outflow from Sgr A* or an outflowing nuclear wind, possibly produced by the young mass-losing stars near Sgr A*. A wind-driven outflow is unlikely to explain the origin of the minicavity and unbound ionized gas unless the outflow is anisotropic with a PA of $\sim 50^\circ$ (and $\sim 230^\circ$) within $14''$ of Sgr A*. One implication of the outflowing material is the prevention of gaseous material falling into the accretion disk of Sgr A*, thus reducing the accretion rate. The proposed hypothesis for a jet from Sgr A* can be tested observationally in the future by searching for linearly polarized emission associated with Sgr A* at radio and submillimeter wavelengths. In addition, future high-resolution proper-motion measurements of C1–C4 toward the minicavity combined with radial velocity measurements will help determine if they are unbound.

Software: CASA (v5.1.1; McMullin et al. 2007).

ORCID iDs

M. J. Royster  <https://orcid.org/0000-0002-5462-7752>
M. Wardle  <https://orcid.org/0000-0002-1737-0871>
D. A. Roberts  <https://orcid.org/0000-0003-4779-8518>

References

Becker, P. A., Das, S., & Le, T. 2011, *ApJ*, **743**, 47
Bradford, C. M., Stacey, G. J., Nikola, T., et al. 2005, *ApJ*, **623**, 866
Christopher, M. H., Scoville, N. Z., Stolovy, S. R., & Yun, M. S. 2005, *ApJ*, **622**, 346
Das, S., Becker, P. A., & Le, T. 2009, *ApJ*, **702**, 649

Eckart, A., Genzel, R., Krabbe, A., et al. 1992, *Natur*, **355**, 526
Ekers, R. D., van Gorkom, J. H., Schwarz, U. J., & Goss, W. M. 1983, *A&A*, **122**, 143
Falcke, H., & Markoff, S. 2000, *A&A*, **362**, 113
Fritz, T. K., Chatzopoulos, S., Gerhard, O., et al. 2016, *ApJ*, **821**, 44
Ghez, A. M., Salim, S., Hornstein, S. D., et al. 2005, *ApJ*, **620**, 744
Gillesen, S., Eisenhauer, F., Trippe, S., et al. 2009, *ApJ*, **692**, 1075
Guesten, R., Genzel, R., Wright, M. C. H., et al. 1987, *ApJ*, **318**, 124
Herbst, T. M., Beckwith, S. V. W., Forrest, W. J., & Pipher, J. L. 1993, *AJ*, **105**, 956
Hernstein, J. R., Moran, J. M., Greenhill, L. J., & Trotter, A. S. 2005, *ApJ*, **629**, 719
Irons, W. T., Lacy, J. H., & Richter, M. J. 2012, *ApJ*, **755**, 90
Jackson, J. M., Geis, N., Genzel, R., et al. 1993, *ApJ*, **402**, 173
Krabbe, A., Genzel, R., Eckart, A., et al. 1995, *ApJL*, **447**, L95
Lacy, J. H., Achtermann, J. M., & Serabyn, E. 1991, *ApJL*, **380**, L71
Latvakoski, H. M., Stacey, G. J., Gull, G. E., & Hayward, T. L. 1999, *ApJ*, **511**, 761
Lebofsky, M. J., Rieke, G. H., & Tokunaga, A. T. 1982, *ApJ*, **263**, 736
Li, Z., Morris, M. R., & Baganoff, F. K. 2013, *ApJ*, **779**, 154
Lo, K. Y., & Claussen, M. J. 1983, *Natur*, **306**, 647
Lu, J. R., Ghez, A. M., Hornstein, S. D., et al. 2009, *ApJ*, **690**, 1463
Lutz, D., Krabbe, A., & Genzel, R. 1993, *ApJ*, **418**, 244
Marshall, J., Lasenby, A. N., & Harris, A. I. 1995, *MNRAS*, **277**, 594
McMullin, J. P., Waters, B., Schiebel, D., Young, W., & Golap, K. 2007, in ASP Conf. Ser. 376, Astronomical Data Analysis Software and Systems XVI, ed. R. A. Shaw, F. Hill, & D. J. Bell (San Francisco, CA: ASP), **127**
Mužić, K., Eckart, A., Schödel, R., et al. 2010, *A&A*, **521**, A13
Mužić, K., Eckart, A., Schödel, R., Meyer, L., & Zensus, A. 2007, *A&A*, **469**, 993
Paumard, T., Genzel, R., Martins, F., et al. 2006, *ApJ*, **643**, 1011
Quataert, E. 2004, *ApJ*, **613**, 322
Reid, M. J., & Brunthaler, A. 2004, *ApJ*, **616**, 872
Roberts, D. A., & Goss, W. M. 1993, *ApJS*, **86**, 133
Roberts, D. A., Yusef-Zadeh, F., & Goss, W. M. 1996, *ApJ*, **459**, 627
Serabyn, E., Lacy, J. H., & Achtermann, J. M. 1991, *ApJ*, **378**, 557
Shcherbakov, R. V., & Baganoff, F. K. 2010, *ApJ*, **716**, 504
Steiner, J. E., Menezes, R. B., & Amorim, D. 2013, *MNRAS*, **431**, 2789
Tsuboi, M., Kitamura, Y., Tsutsumi, T., et al. 2017a, *ApJL*, **850**, L5
Tsuboi, M., Kitamura, Y., Uehara, K., et al. 2017b, *ApJ*, **842**, 94
Wang, Q. D., Nowak, M. A., Markoff, S. B., et al. 2013, *Sci*, **341**, 981
Wilson, T. L., Rohlfs, K., & Huttemeister, S. 2012, Tools of Radio Astronomy (5th ed.; Berlin: Springer)
Wollman, E. R., Smith, H. A., & Larson, H. P. 1982, *ApJ*, **258**, 506
Yuan, F., Quataert, E., & Narayan, R. 2004, *ApJ*, **606**, 894
Yusef-Zadeh, F., Arendt, R., Bushouse, H., et al. 2012, *ApJL*, **758**, L11
Yusef-Zadeh, F., & Morris, M. 1991, *ApJL*, **371**, L59
Yusef-Zadeh, F., Morris, M., & Ekers, R. D. 1990, *Natur*, **348**, 45
Yusef-Zadeh, F., Roberts, D. A., & Biretta, J. 1998, *ApJL*, **499**, L159
Yusef-Zadeh, F., Wardle, M., Schödel, R., et al. 2016, *ApJ*, **819**, 60
Zhao, J.-H., Blundell, R., Moran, J. M., et al. 2010, *ApJ*, **723**, 1097
Zhao, J.-H., Morris, M. R., Goss, W. M., & An, T. 2009, *ApJ*, **699**, 186